



Cite this: DOI: 10.1039/d0ta07796h

Z-Scheme 2D/3D hierarchical MoS₂@CoMoS₄ flower-shaped arrays with enhanced full spectrum light photoelectrocatalytic activity for H₂O₂/*p*-aminophenol production and contaminant degradation†

Ao Zhang, Lijun Yang and Lei Zhang *

Developing high-performance catalysts for converting naturally existing simple molecules/poisonous chemicals into value-added commodity chemicals with environmental and socioeconomic benefits is a great challenge. Herein, Z-scheme 2D/3D hierarchical MoS₂@CoMoS₄ flower-shaped arrays as dual-functional electrodes for photoelectrocatalytic (PEC) hydrogen peroxide (H₂O₂)/*p*-aminophenol (*p*-AP) production and lomefloxacin (LOM) degradation were fabricated via a strategy of merging 2D MoS₂ nanosheets into the nano-leaves of 3D CoMoS₄ micro-flowers. MoS₂@CoMoS₄ as a photocathode provides a green, economic and efficient route to achieve photoelectric-driven high productivity toward H₂O₂ (about 205 μM of H₂O₂ was produced under irradiation for 120 min) and *p*-AP (the corresponding *p*-AP yield was about 83% under illumination for 180 min) by using 5.0 mg of catalyst without any co-catalyst, while as a photoanode it also exhibits enhanced PEC performance for LOM oxidative degradation. The improved photoelectro-chemical redox activity is primarily attributed to the formation of a Z-scheme charge-transfer path, which can restrain the recombination of charges and lead to significantly enhanced redox ability of excited e⁻ and h⁺. The unique 2D/3D hierarchical MoS₂@CoMoS₄ flower-shaped arrays can economically achieve maximal harvesting of solar energy and full-spectrum light absorption, and provide more active sites, thus synergistically enhancing the catalytic performance. This work is instructive for the design of efficient bifunctional photoelectrocatalysts for meeting demands for chemical resources and concerns about environmental remediation through constructing a Z-scheme heterostructure photoelectrocatalyst.

Received 8th August 2020
Accepted 18th November 2020

DOI: 10.1039/d0ta07796h

rsc.li/materials-a

Introduction

With the unscientific use of non-renewable energy sources and the development it has sparked in industry and agricultural production, the global energy crisis and environmental deterioration have become increasingly serious, which are also the main challenges facing mankind at present. As one of the cleanest, richest and greenest sources of energy, solar energy is of great significance to alleviate the increasingly serious energy crisis in modern industry.^{1,2} In particular, generating H₂O₂,³ H₂ and O₂,⁴ removing organic/inorganic contaminants,⁵ and sunlight-driven catalytic reactions can be carried out efficiently, which is an ideal way to realize green chemistry, and resolve the energy and environmental problems. Compared with H₂ and O₂, H₂O₂ can be more safely stored and transported due to its

water solubility.³ H₂O₂ as a kind of cleaning oxidant is not only a substitute for hydrogen in single-cell battery power generation but also has low cost and minimal environmental impact, particularly since its only by-product is water.⁶ Therefore, the green production of H₂O₂ has attracted more and more attention, because traditional methods for producing H₂O₂, such as the anthraquinone method, are limited by their high costs and toxic by-products involved in multi-step chemical reactions. Thus, there is an urgent need to find a high-performance, cost-effective and renewable green method to produce H₂O₂.

There are usually two possible synthesis routes for H₂O₂, both the oxygen reduction reaction (ORR) at the cathode and the water oxidation reaction (WOR) at the anode. However, the WOR itself has been extremely challenging up to now due to the uphill thermodynamics (1.76 V) together with sluggish kinetics and the generation of by-product O₂ with kinetic advantages (1.23 V). Therefore, the production of H₂O₂ through ORR under acidic conditions has been extensively studied.^{7,8}

At present, some researchers use noble metals and their alloys (for example Pd-Hg,⁹ Pt-Hg¹⁰ and Pd-Au¹¹), or corresponding hybrids (Pt/TiN,¹² Pt/CuS_x¹³) as electrocatalysts for the

College of Chemistry, Liaoning University, 66 Chongshan Middle Road, Shenyang, Liaoning, 110036, People's Republic of China. E-mail: zhanglei63@126.com; Fax: +86 24 62202380; Tel: +86 24 62207809

† Electronic supplementary information (ESI) available. See DOI: 10.1039/d0ta07796h

high-selectivity synthesis of H_2O_2 in the electrocatalysis field but they suffer from high cost, which makes them unsuitable in commercial applications. There is still a lack of an efficient cheap catalyst to selectively reduce O_2 to H_2O_2 , especially in acidic environments.¹⁴ Furthermore, the electrocatalytic production of H_2O_2 *via* ORR is also restricted owing to its high energy consumption.

Photocatalytic “green” technology has attracted growing research as an alternative method of solar energy storage and capture, and has displayed potential applications in green synthesis and oxidative degradation.¹⁵ The advantages of photocatalysis for ORR and WOR to H_2O_2 are low energy consumption, cleanliness and safety. At present, the search for a catalyst for the photocatalytic production of H_2O_2 is mainly concentrated on various modified $\text{g-C}_3\text{N}_4$ materials. Some researchers reported that various modified $\text{g-C}_3\text{N}_4$ photocatalysts, such as silver-decorated ultrathin $\text{g-C}_3\text{N}_4$ nanosheets,¹⁶ mellitic triimide-doped $\text{g-C}_3\text{N}_4$,¹⁷ biphenyl diimide doped $\text{g-C}_3\text{N}_4$,¹⁸ Ti_3C_2 MXene/porous $\text{g-C}_3\text{N}_4$,¹⁹ pyromellitic diimide incorporated $\text{g-C}_3\text{N}_4$,²⁰ nitrogen-vacancy and carbon-vacancy enriched $\text{g-C}_3\text{N}_4$ ²¹ and benzene-substituted $\text{g-C}_3\text{N}_4$ ²² have shown enhanced H_2O_2 production through photocatalytic technology. However, the low yield of photocatalytic production of H_2O_2 is still far from satisfactory due to the rapid recombination of e^- - h^+ after excitation, and the homogeneous photocatalyst is difficult to separate and recycle from the H_2O_2 product, so the types of effective catalysts are scarce. To overcome the photocatalyst recombination and the problems of recycling powder catalysts and so on, the sunlight-driven PEC technique has been proven to be an effective way to promote the separation of photo-generated e^-/h^+ pairs and enhance the catalytic property.

Recently, PEC technology has been widely used in the reduction of CO_2 ,²³ the production of H_2 and O_2 ,²⁴ as well as in the degradation of organic pollutants.⁵ The promising PEC reaction is highly dependent on catalysts with a suitable band gap energy, good sunlight-harvesting ability, efficient separation and long charge-carrier lifetime. Transition-metal sulfides generally have superior photoelectric properties and relative narrow band energy, and they favor adsorption of molecular oxygen due to the presence of sulfur,²⁵ which accelerates the catalytic reaction process by modulating the electron transfer numbers in ORR.^{26,27}

The construction of a Z-scheme heterostructure has been paid much attention by researchers because of its more advantageous charge-carrier transfer mechanism. The Z-scheme model not only significantly promotes the separation efficiency of photo-induced e^- and h^+ pairs, but also maintains the stronger redox ability of photo-generated e^- and h^+ , which will result in enhanced PEC performance. So far Z-scheme metal sulfide heterostructures, such as CdS/CdO ,²⁸ $\text{Bi}_2\text{S}_3/\text{MoS}_2/\text{TiO}_2$ ²⁹ and $\text{ZnIn}_2\text{S}_4/\text{TiO}_2$,³⁰ have successfully displayed potential applications in various scientific activities for the production and storage of energy, in various devices and for environmental pollution abatement. To our knowledge, there has not been a study on proposing and fabricating 3D hierarchical Z-scheme heterojunction composites with the aim of PEC production of H_2O_2 . It was previously reported that compared with crystalline Mo-based material, amorphous Mo-based materials, especially ternary transition metal sulfide, have

greatly improved PEC activity for HER due to the fact that unsaturated sites and surface defects can expose more active sites.^{31,32} Therefore, embedding crystalline MoS_2 in amorphous CoMoS_4 might achieve maximal harvesting of solar energy and full-spectrum light absorption. It is worth noting that both MoS_2 and CoMoS_4 had a matched band gap for PEC applications, as well as common elements Mo and S, which inspired us to fabricate a 3D hierarchical $\text{MoS}_2@/\text{CoMoS}_4$ Z-scheme heterojunction catalyst to give it a multifunctional purpose for the production of $\text{H}_2\text{O}_2/p\text{-AP}$ and the degradation of pollutants.

Hence, in this study a novel 3D hierarchical flower-shaped $\text{MoS}_2@/\text{CoMoS}_4$ Z-scheme hybrid was successfully prepared by a simple solvothermal synthetic method. It should be noted that the 3D hierarchical structure was constructed by integrating 2D nanosheets and 3D micro-flowers, which combined the merits of both materials. The fabricated Z-scheme 3D $\text{MoS}_2@/\text{CoMoS}_4$ composite was successfully applied for visible-light-driven PEC production of value-added commodity chemicals of $\text{H}_2\text{O}_2/p\text{-AP}$, as well as the degradation of LOM, and the mechanism of photoelectrocatalysis is revealed in detail. Owing to its superior features, 3D $\text{MoS}_2@/\text{CoMoS}_4$ could be engaged in some scientific activities for energy production and environmental pollution treatment.

2. Experiment section

2.1 Chemicals

$\text{CoCl}_2 \cdot 6\text{H}_2\text{O}$, $(\text{NH}_4)_6\text{Mo}_7\text{O}_{24} \cdot 4\text{H}_2\text{O}$, $\text{Na}_2\text{S} \cdot 9\text{H}_2\text{O}$, NH_4F , $\text{CO}(\text{NH}_2)_2$, thiourea ($\text{CH}_4\text{N}_2\text{S}$), *p*-aminophenol (*p*-AP), *p*-nitrophenol (*p*-NP) and lomefloxacin (LOM) were obtained from Sinopharm Chemical Reagent Co., Ltd (China), and carbon cloth was provided by Suzhou Dasheng Electronic Materials Co., Ltd (China).

2.2 Catalysts and photoelectrode preparation

Synthesis of 3D CoMoS_4 micro-flowers. The CoMoS_4 micro-flowers were fabricated according to the following method: $\text{CoCl}_2 \cdot 6\text{H}_2\text{O}$ (0.5 mmol), $(\text{NH}_4)_6\text{Mo}_7\text{O}_{24} \cdot 4\text{H}_2\text{O}$ (0.071 mmol), $\text{CO}(\text{NH}_2)_2$ (5 mmol), $\text{Na}_2\text{S} \cdot 9\text{H}_2\text{O}$ (3 mmol) and NH_4F (2.5 mmol) were dissolved in 36 mL of deionized (DI) water and stirred to form a clear solution at room temperature. The as-formed homogenous solution was then transferred into a Teflon-lined steel autoclave, which was sealed, maintained at 120 °C for 12 h, and then naturally cooled to room temperature. The product was collected by centrifugation at 4000 rpm for 5 min, washed a few times with DI water and ethanol, and then dried at 60 °C for 12 h.

Synthesis of $\text{MoS}_2@/\text{CoMoS}_4$. 0.149 g of CoMoS_4 , 0.5 mmol of $(\text{NH}_4)_6\text{Mo}_7\text{O}_{24} \cdot 4\text{H}_2\text{O}$ and 15 mmol of thiourea were dispersed and dissolved in 35 mL of DI water, magnetically stirred for 20 min, and then transferred to a Teflon-lined steel autoclave with a volume of 50 mL and heated at 180 °C for 24 h. Subsequently, the autoclave was naturally cooled down to room temperature.

For comparison, pure MoS_2 was also obtained using the same method (heating at 180 °C for 24 h).

Construction of photoelectrode. A 3D MoS₂@CoMoS₄ flower-like array electrode was synthesized as follows: firstly, carbon cloths with an average size of 2 × 3 cm² were pretreated on the basis of previous work.³³ Subsequently, 1 mL of solution containing 5 mg of MoS₂@CoMoS₄ (5 mg mL⁻¹) was uniformly deposited onto a carbon cloth (2 × 2 cm²) and dried at 60 °C for 2 h to form a uniform film. All examined photoelectrodes were fabricated by the same method.³⁴

2.3 Material characterization

A scanning electron microscope (SEM, SU8000, Hitachi Co., Japan) and transmission electron microscope (TEM, Oxford, TSR, USA) with an EDS detector attached were operated to investigate the morphology, structure and chemical information of the as-prepared materials. X-ray photoelectron spectroscopy (XPS, Thermo Electron, ESCALAB 250 Xi., USA) was used to analyze the chemical state of the samples. Powder X-ray diffraction patterns/Raman spectra were collected on a diffractometer (XRD, D5000, Siemens Co., Germany)/micro-Raman spectra (Renishaw inVia system equipped with an integral microscope (Leica)). A UV-vis spectrophotometer (Shimadzu, UV-2600) was used to record the UV-vis diffuse reflectance spectra (DRS) of the prepared samples. Photoluminescence (PL) spectra of the samples were collected on a fluorescence spectrometer (RF-5301PC, SHIMADZU, Japan). The electron spin resonance (ESR) signals of the radicals were collected on a Bruker ER200-SRC instrument. Electrochemical impedance spectra (Nyquist plots) of the different samples in 50 mM of K₃[Fe(CN)₆] solution was collected by applying 5 mV amplitude in a frequency range from 10 000 to 0.1 Hz and recorded at open circuit potential.

All electrochemical measurements were performed in the standard three-electrode system by a computer-controlled workstation (CHI 660D, Shanghai ChenHua Instruments Co., China).

2.4 Photoelectrochemical tests

PEC H₂O₂/p-AP production. The PEC activity of the catalyst as a photocathode (at -0.5 V bias voltage (vs. SCE)) was

evaluated by H₂O₂/p-AP production under a 300 W xenon lamp with a 420 nm cutoff filter at 100 mW cm⁻². The initial pH was adjusted to 3.0 with 1.0 M HClO₄ (if producing H₂O₂, the O₂ was continuously bubbled into the 0.1 M Na₂SO₄ solution; when producing p-AP, the solution was 0.1 M Na₂SO₄ containing 10 mg L⁻¹ p-NP), and then the prepared photoelectrode was put into the electrolytic cell for 30 min ensuring the adsorption-desorption equilibrium of the solution before irradiation. The evolved H₂O₂/p-AP was monitored by KMnO₄ redox titration/HPLC (Shimadzu LC-16, Japan) equipped with an SB-C18 column (4.6 mm × 150 mm, 5 μm) using a VWD detector at 290 nm; the flow rate of the mobile phase was 1.0 mL min⁻¹, and the mobile phase was methanol/water (60/40, v/v). The initial concentration (pH = 3) of H₂O₂ was selected as 2 mM to investigate the decomposition behavior of H₂O₂ over the photocathode under irradiation for 120 min.

PEC LOM degradation. The PEC performance of the catalyst as a photoanode (at 0.8 V bias voltage (vs. SCE)) was investigated by the degradation of LOM (5 mg L⁻¹) in 0.1 M Na₂SO₄ supporting electrolyte (pH = 10) under a 300 W xenon lamp at 100 mW cm⁻². The adsorption-desorption equilibrium was reached after 30 min in the dark; 3 mL of aliquot was separated and used to monitor the concentration of targets with a spectrophotometer (Shimadzu UV-2550, Japan) in the same time interval. After the measurement, the aliquots were promptly poured back into the reaction system.

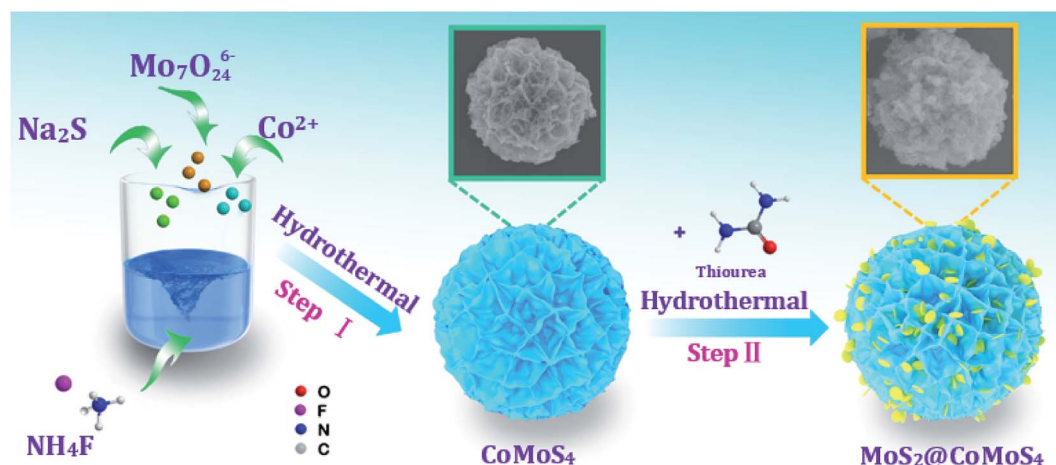
2.5 Free radical trapping experiments

The process was the same as the PEC activity test mentioned above except for adding scavengers. During the PEC reaction, (NH₄)₂C₂O₄ (AO), AgNO₃, p-benzoquinone (PBQ) and isopropyl alcohol (IPA)³⁵ were used to capture h⁺, e⁻, ·O₂⁻ (e⁻ + O₂ → ·O₂⁻) and ·OH, respectively.³⁶

3. Results and discussion

3.1 Catalyst characterization

The fabrication schematic diagram of the 2D/3D MoS₂@CoMoS₄ heterojunction is shown in Scheme 1. The 2D MoS₂ nanosheets were successfully merged into the nano-leaves of 3D



Scheme 1 The preparation process of MoS₂@CoMoS₄.

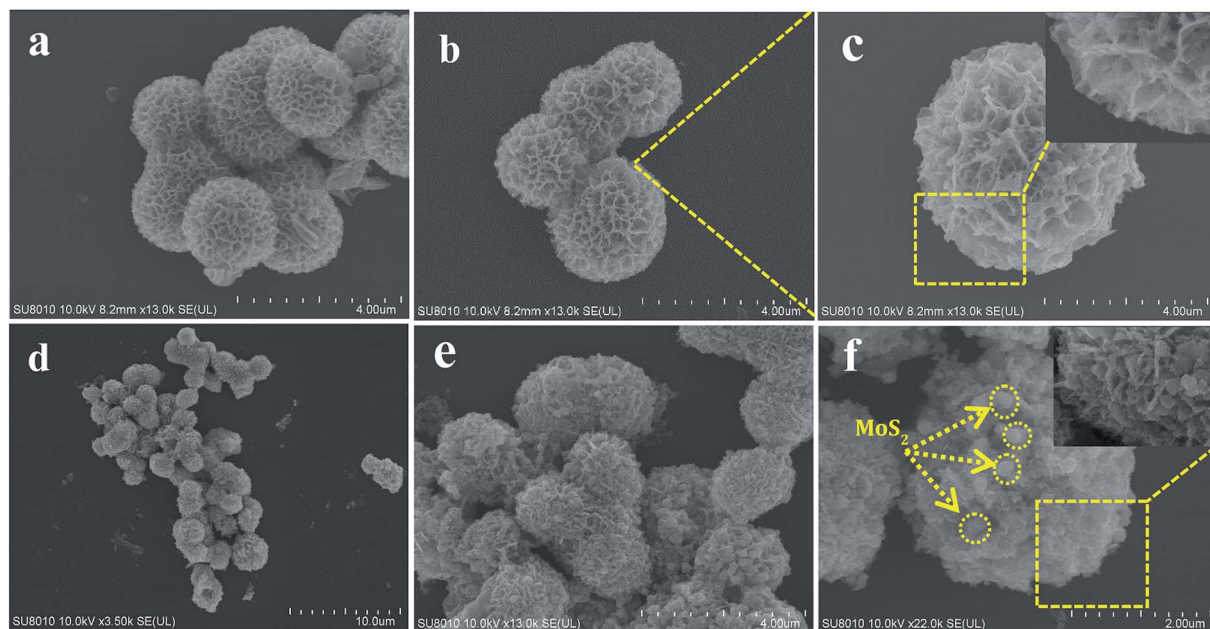


Fig. 1 (a–c) SEM images of CoMoS_4 micro-flowers; (d–f) SEM images of 2D/3D hierarchical $\text{MoS}_2@CoMoS_4$.

CoMoS_4 micro-flowers by a simple two-step hydrothermal method.

As shown in the SEM images in Fig. 1a–c, 3D CoMoS_4 with a uniform hierarchical flower-shaped structure and an average size of about $3\ \mu\text{m}$ was assembled from 2D CoMoS_4 nanosheets, which crossed each other to form a large amount of open-free space in the micro-flower which would significantly enlarge

the specific surface area of CoMoS_4 . Moreover, each nanosheet as a support could offer a good contact interface to load other semiconductors in forming heterojunction hybrids. The SEM images of 2D/3D $\text{MoS}_2@CoMoS_4$ are shown in Fig. 1d–f, where uniform growth of the few-layered 2D MoS_2 flakes is interspersed into the surface of 3D CoMoS_4 , which proved that 2D MoS_2 was successfully assembled on the surface of CoMoS_4 via

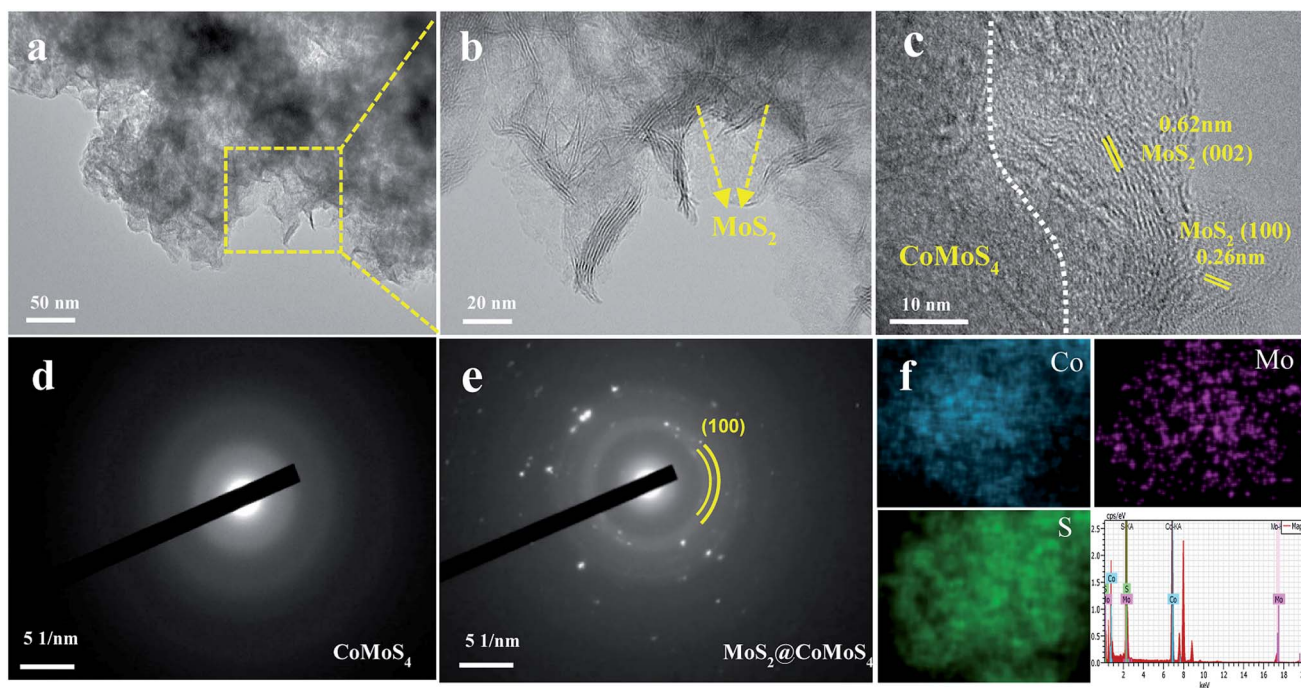


Fig. 2 TEM image of $\text{MoS}_2@CoMoS_4$ (a), enlarged TEM image of the nanosheet edge (b) and HRTEM image of MoS_2 encapsulated at the edge of CoMoS_4 (c); SAED spectrum of amorphous CoMoS_4 (d) and 2D/3D hierarchical $\text{MoS}_2@CoMoS_4$ (e); EDS elemental mapping of Co, Mo and S of the $\text{MoS}_2@CoMoS_4$ (f).

the hydrothermal process. The SEM image of the pure MoS₂ nanosheets stacked is also shown in Fig. S1.†

The detailed structure and morphology of the as-prepared composites were further revealed by TEM. As shown in Fig. 2a, the edges of the MoS₂@CoMoS₄ composites exhibited a large number of obvious nanosized flake-like structures. The curled flaky edges were selected for further magnification, revealing that hybrids of CoMoS₄ nanosheet-supported MoS₂ (2D MoS₂@2D CoMoS₄) were synthesized. The MoS₂ nanosheets were uniformly distributed on the CoMoS₄ nanosheets, leading to a large specific surface area and good electrical conductivity (Fig. 2b). In addition, dense interconnected ripples could also be observed, suggesting the edge-rich feature of the MoS₂ nanosheets. The HRTEM image in Fig. 2c further showed that the composite was composed of CoMoS₄ and MoS₂. Two different lattice fringes with d-spacings of 0.26 and 0.62 nm could be assigned to the (100) and (002) planes, respectively, of MoS₂. Furthermore, only a few discontinuous lattice fringes were observed at the edge of the interface, and they gradually became inconspicuous or even disappeared, indicating that CoMoS₄ might be an amorphous and rich-defect structure. The corresponding selected area electron diffraction (SAED) spectrum with extremely blurry diffraction rings in Fig. 2d further showed that the CoMoS₄ exhibited an amorphous structure, while in the SAED spectrum (Fig. 2e) of the MoS₂@CoMoS₄ array, the discernible ring was indexed to the (100) plane of MoS₂, further proving the successful assembly of MoS₂, which was consistent with the subsequent results of XRD. According to the EDS elemental mapping in Fig. 2f, this confirmed a uniform distribution of Co, Mo and S elements throughout the MoS₂@CoMoS₄ sample. These results confirmed the successful preparation of 2D/3D hierarchical MoS₂@CoMoS₄ arrays.

The detailed crystal structures of the prepared samples were studied by XRD. The XRD patterns of MoS₂@CoMoS₄, pristine CoMoS₄ and MoS₂ were exhibited in Fig. 3a. As shown in the XRD diagram of pristine CoMoS₄, no diffraction peaks were presented, which implied that the CoMoS₄ structure was amorphous and consistent with the result reported in the literature.³⁷ Clearly, the MoS₂ showed broad and short diffraction peaks consistent with JCPDS no. 37-1492,³⁸ indicating the purity of the as-prepared MoS₂, the smaller average crystallite size and layers and well-stacked lamellar structure. After the formation of the MoS₂@CoMoS₄ composite, except for the corresponding MoS₂ peak (002), the remaining peaks (100, 110) were clearly verified, which may be due to the lower content of MoS₂.

In order to confirm the successful growth of MoS₂ on CoMoS₄, the Raman spectra were investigated and were shown in Fig. 3b. The band at 924 cm⁻¹ corresponded to the Mo–S symmetric stretching mode. The bands at 868 cm⁻¹ and 806 cm⁻¹ were associated with the S asymmetric stretching mode of the S–Mo–S bond. The band at 404 cm⁻¹ was attributed to the out-of-plane vibration of S atoms in opposite directions. The band at 360 cm⁻¹ could be associated with the Co–S–Mo symmetric stretching mode. In the Raman spectrum of MoS₂@CoMoS₄, two new bands appearing at 376 cm⁻¹ and 404 cm⁻¹, respectively, could be assigned to the E_{2g} and A_{1g}

vibration modes of the MoS₂, indicating that the MoS₂@CoMoS₄ composite photoelectrocatalyst was successfully prepared.³⁹ Raman analysis further proved the effective combination of the two semiconductors to form MoS₂@CoMoS₄ heterojunctions.

XPS was employed to further characterize the chemical composition of MoS₂@CoMoS₄. Signals of Co, Mo and S could be detected in the survey spectrum (Fig. 3c). The Co 2p spectrum exhibited five peaks including one at about 779.11 eV belonging to the CoMoS phase (Co–Mo–S), two peaks at 781.34 and 797.68 eV belonging to Co 2p_{3/2} and Co 2p_{1/2}, and another two peaks at 794.09 and 802.77 eV denoted as Sat., suggesting that Co²⁺ ions were bonded with [MoS₄]²⁻ (Fig. 3d).^{40–42} The high-resolution spectrum of Mo 3d showed a small peak at the position of 235.32 eV (Mo 3d_{5/2}), which was consistent with Mo⁶⁺ in the (NH₄)₆Mo₇O₂₄ precursor, while the peaks at 228.77 and 232.16 eV could demonstrate the existence of Mo⁴⁺ (Fig. 3e).⁴⁰ The peak located at 226.12 eV corresponded to the chemical state of S 2s of MoS₂, which was consistent with the previous analysis.⁴³ The measured S 2p peaks were located at 161.68 and 162.88 eV, which could be indexed as the S 2p_{3/2} and S 2p_{1/2} binding energies from the typical Co–S bonds, respectively, revealing that the chemical oxidation state of S was the –2 state for CoMoS₄ (Fig. 3f). Meanwhile, the peak for S 2p_{3/2} at 164.08 eV indicated the presence of bridging apical S²⁻ for MoS₂.^{43–45} The results of the XPS analysis confirmed the successful formation of MoS₂@CoMoS₄ heterojunctions.

The DRS UV-vis spectra of 2D MoS₂, 3D CoMoS₄ and 2D/3D MoS₂@CoMoS₄ were shown in Fig. 4a. Obviously, compared to pristine 3D CoMoS₄, pure 2D MoS₂ nanosheets had a strong visible light absorption intensity (400–1000 nm). After the formation of an MoS₂@CoMoS₄ heterojunction, the visible light absorption intensity was further improved. The increased light absorption intensity was beneficial for the utilization of visible light, so it was expected to exhibit better visible-light-driven PEC activity. Moreover, the band gap values (E_g) of MoS₂ and CoMoS₄ were estimated to be 1.28 eV and 2.76 eV, respectively (Fig. 4b) by the Kubelka–Munk theorem.

The semiconductor types and band-edges of pure MoS₂ and CoMoS₄ can be acquired from the Mott–Schottky (M–S) results. Usually, a linear plot with a positive slope indicates that the material is an n-type semiconductor, while a negative slope indicates that the material is a p-type semiconductor.⁴⁶ It could be observed from Fig. 5a and b that MoS₂ and CoMoS₄ were both n-type semiconductors and the corresponding flat band (f_b) values were calculated as –0.35 eV vs. SCE (–0.11 eV vs. NHE, E_{NHE} = E_{SCE} + 0.24) and –0.13 eV vs. SCE (0.11 eV vs. NHE), respectively.^{47,48} Moreover, the edge position of f_b is 0.1–0.3 eV higher than the conduction band (E_{CB}) of the n-type semiconductor.⁴⁹ Therefore, the E_{CB} values of MoS₂ and CoMoS₄ were –0.41 eV (vs. NHE) and –0.19 eV (vs. NHE), respectively. According to the formula (E_g = E_{VB} – E_{CB}) and the E_g of MoS₂ and CoMoS₄ in Fig. 4b, the E_{VB} value of MoS₂ and CoMoS₄ could be further calculated to be 0.87 eV (vs. NHE) and 2.57 eV (vs. NHE), respectively. The relative approximate energy band diagrams of CoMoS₄ and MoS₂ were shown in Fig. 5c.

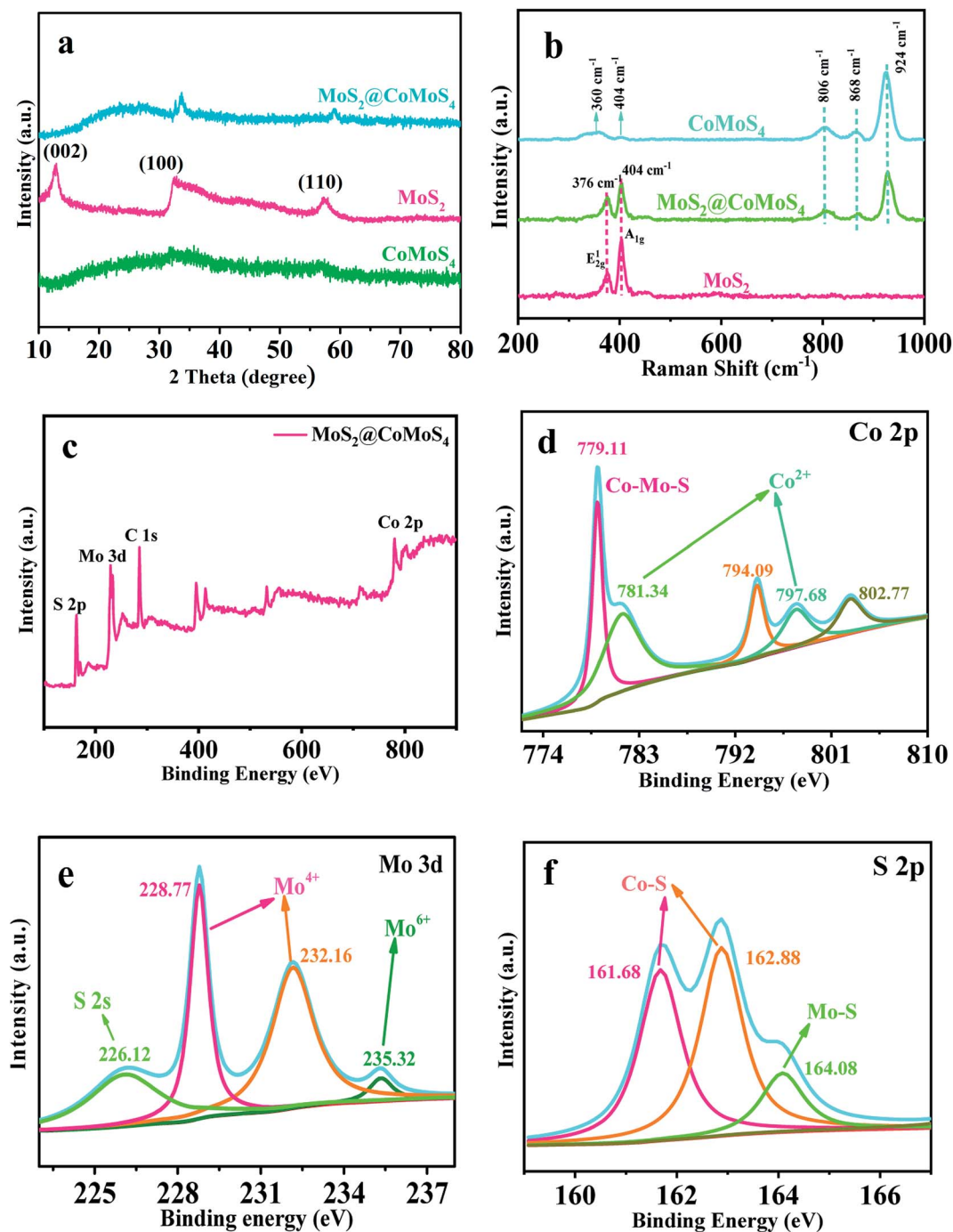


Fig. 3 XRD patterns of the as-prepared samples (a); Raman spectra of CoMoS₄, MoS₂ and MoS₂@CoMoS₄ (b); XPS spectra of MoS₂@CoMoS₄ (c), Co 2p (d), Mo 3d (e) and S 2p (f).

In order to find the separation efficiency and lifetime of the photogenerated e^-/h^+ , a photoelectrochemical test of the samples was carried out. As shown in the amperometric $I-t$ curves in Fig. 6a, the MoS₂@CoMoS₄ heterojunctions exhibited the highest photocurrent response compared to pristine MoS₂ and CoMoS₄, indicating that the composites have the highest separation efficiency of photo-generated e^-/h^+ pairs, which might be attributed to the MoS₂@CoMoS₄ heterojunction formed by the proper contact surface. Meanwhile,

electrochemical impedance spectra (EIS) measurement was used to investigate the charge transfer resistance (R_{ct}) and separation efficiency of photo-generated e^-/h^+ pairs. The formed MoS₂@CoMoS₄ heterojunction had a smaller arc radius ($R_{ct} \approx 62 \Omega$) than pristine CoMoS₄ ($R_{ct} \approx 127 \Omega$), indicating that the MoS₂@CoMoS₄ heterojunction had an improved interface charge transfer rate (Fig. 6b). The standard Randle's equivalent circuit model, including a constant phase element (CPE), charge transfer resistance value (R_{ct}), Warburg impedance (Z_w)

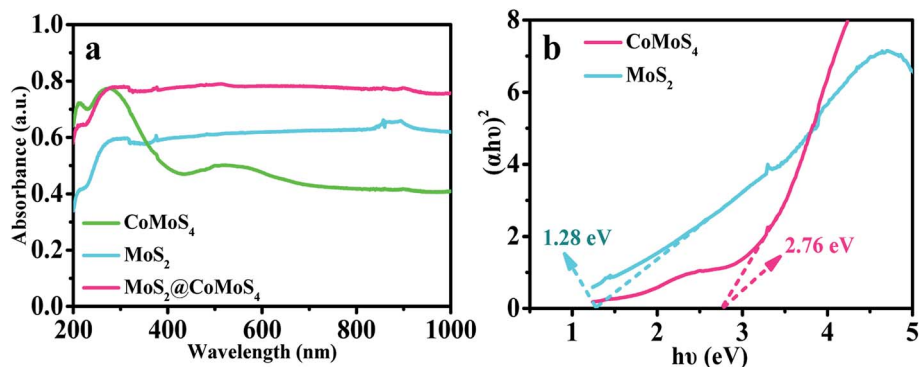


Fig. 4 (a) UV-vis absorption spectra; (b) plots of $(\alpha h\nu)^2$ versus the photon energy ($h\nu$) of MoS_2 and CoMoS_4 , respectively.

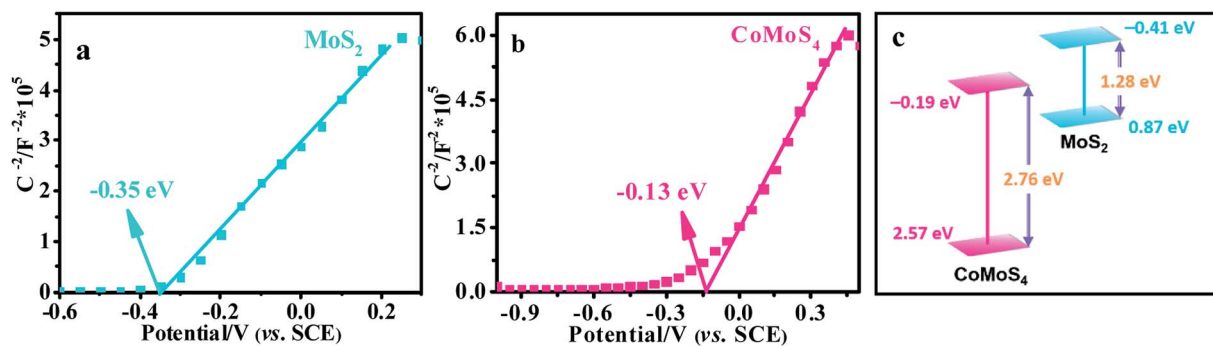


Fig. 5 The Mott-Schottky plots of (a) MoS_2 and (b) CoMoS_4 in 0.1 M Na_2SO_4 solution; (c) energy-band diagram of CoMoS_4 and MoS_2 .

and the uncompensated solution resistance (R_s), was used to fit the impedance data. The above $I-t$ curves of photocurrent and EIS experimental results proved that the $\text{MoS}_2@\text{CoMoS}_4$ heterojunction had a higher carrier separation efficiency and faster interfacial charge transfer.

The PL spectra (Fig. 6c) of CoMoS_4 and $\text{MoS}_2@\text{CoMoS}_4$ with an excitation wavelength of 310 nm were employed to further investigate the separation and recombination efficiency of photo-generated carriers. Clearly, the PL emission intensity of $\text{MoS}_2@\text{CoMoS}_4$ (365 nm) was weaker than that of pure CoMoS_4 , indicating that higher separation efficiency and faster interfacial charge transfer existed in the $\text{MoS}_2@\text{CoMoS}_4$ heterojunction, which was conducive to enhancing its PEC activity.⁵⁰

Fig. 6d shows the light-on and light-off current-potential curve. The increase in current under illumination indicated that $\text{MoS}_2@\text{CoMoS}_4$ had a better photoelectric performance with either positive or negative bias potential exerted. That is to say, the composite catalyst might be used as both a photocathode and a photoanode.

3.2 PEC specialized for $\text{H}_2\text{O}_2/p\text{-AP}$ production using $\text{MoS}_2@\text{CoMoS}_4$ photocathode

PEC for H_2O_2 production is an attractive strategy to address chemical resource demands. To investigate H_2O_2 generation, the PEC process was conducted in O_2 dissolved in water without any co-catalyst or sacrificial agent using a standard three-electrode system at an optimal applied bias of -0.5 V (vs.

SCE) (Fig. S2†) and illumination. Fig. 7a displayed an efficient visible-light-driven PEC performance on H_2O_2 production with different photoelectrocatalysts as photocathode. It was found that 2D/3D hierarchical $\text{MoS}_2@\text{CoMoS}_4$ produced more H_2O_2 than 2D MoS_2 or 3D CoMoS_4 due to enhanced optical absorption, charge-carrier separation and transfer. An H_2O_2 concentration of 205 μM could be achieved after 120 min of visible light irradiation, which was about 1.86 and 2.93 times that of CoMoS_4 (110 μM) and MoS_2 (70 μM). PEC activity was also dependent on 2D MoS_2 modifying dosage (Fig. S3†): H_2O_2 production on the modified CoMoS_4 increased with an increase in MoS_2 dosage due to its favorable effects on enhancing visible light absorption. Nevertheless, excess surface modifier would cover some catalytic sites and decrease the approachability of O_2 , resulting in a reduction in H_2O_2 production.

Meanwhile, control experiments (Fig. 7b) revealed that H_2O_2 could hardly be detected in the absence of O_2 environment and visible light radiation, indicating that O_2 and visible light catalysis were especially indispensable for the PEC H_2O_2 production process. Moreover, the photoelectric-driven formation of H_2O_2 might also depend on the pH of the aqueous solution, because H_2O_2 generation might be a proton-coupled electron transfer process on the photocathode. The pH values of the PEC reaction system were investigated (pH = 2, 3 and 5) by adjusting with HClO_4 solution in the presence of catalysts. From Fig. 7c, it was observed that the amount of H_2O_2 attained its maximum when pH = 3, while the H_2O_2 decreased relatively

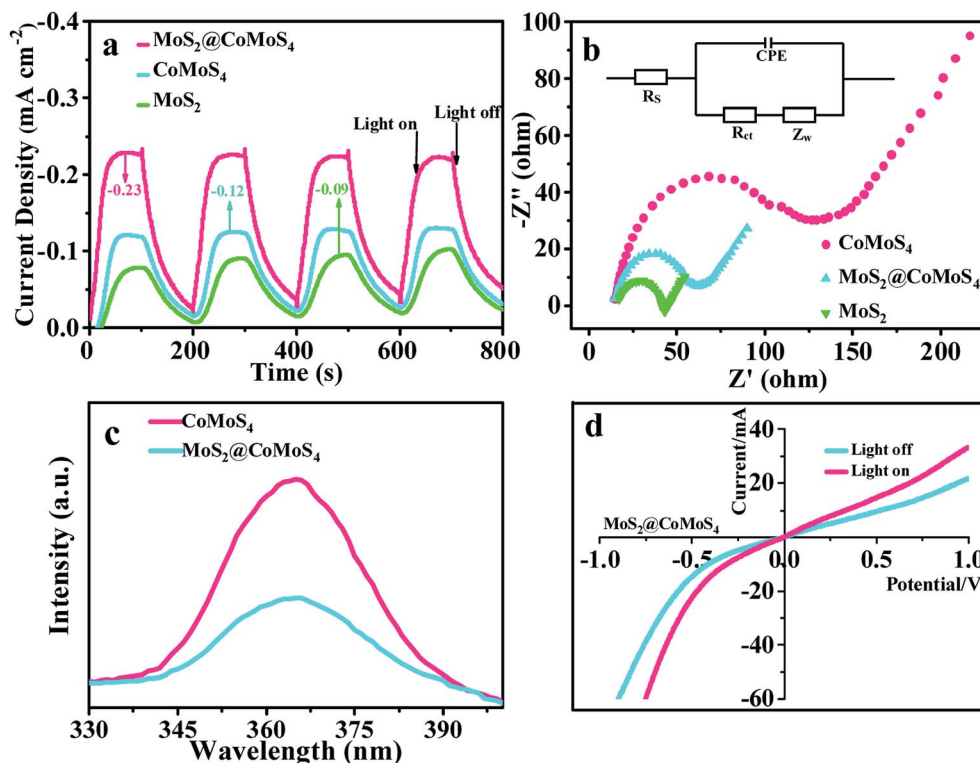


Fig. 6 (a) The periodic on/off photocurrent response at -0.5 V bias potential vs. SCE; (b) electrochemical impedance spectra (Nyquist plots) of the different samples; (c) photoluminescence spectra of prepared samples; (d) the light-on and light-off current–potential curve (0.1 M Na_2SO_4 aqueous solutions).

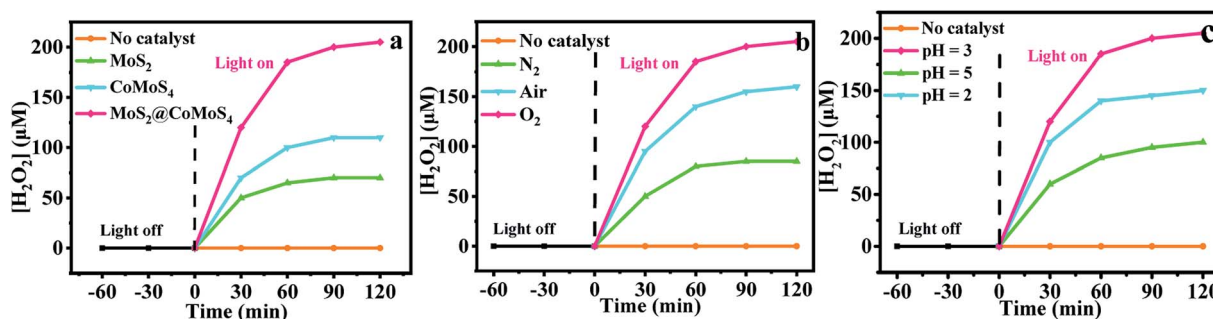


Fig. 7 PEC-driven H_2O_2 production over different catalysts (a); the PEC activity of 3D $\text{MoS}_2@\text{CoMoS}_4$ in different gas environments (b) and at different pH (c).

in content when the pH decreased to 2 or increased to 5, suggesting that it might be attributed to the excess protons that induced the gradual oxidation of the produced H_2O_2 into H_2O ($\text{H}_2\text{O}_2 + 2\text{H}^+ + 2\text{e}^- \rightarrow 2\text{H}_2\text{O}$) or a less proton-rich environment leading to lower H_2O_2 production, which showed that pH = 3 was the optimum pH value for PEC production of H_2O_2 . In summary, under the conditions of pH = 3, visible light irradiation, oxygen environment and -0.5 V bias voltage, the photoelectric-driven H_2O_2 yield by the composite material $\text{MoS}_2@\text{CoMoS}_4$ reached its maximum.

Fig. 8a shows the free radical trapping experiments for the synthesis of H_2O_2 . It could be found that the amount of H_2O_2 generated decreased significantly after adding an e^- scavenger

(AgNO_3), while the production of H_2O_2 would increase after the addition of an h^+ scavenger (AO), because adding an h^+ scavenger would increase the utilization efficiency of e^- or inhibit the decomposition reaction of H_2O_2 , which indicated that the participation of e^- was crucial in the production process of H_2O_2 . Combining with the above experiments, O_2 , H^+ and e^- all affected the amount of H_2O_2 generated in this experiment, so it was speculated that the synthesis of H_2O_2 may be an ORR of proton-coupled electron transfer. In order to further explore the detailed electron transfer path of the ORR, *p*-benzoquinone (PBQ, 1 mM) was added to scavenge $\cdot\text{O}_2^-$. As shown in Fig. 8a, less than 24% of the H_2O_2 production decreased in the $\text{MoS}_2@\text{CoMoS}_4$ system, indicating that $\cdot\text{O}_2^-$ might affect the

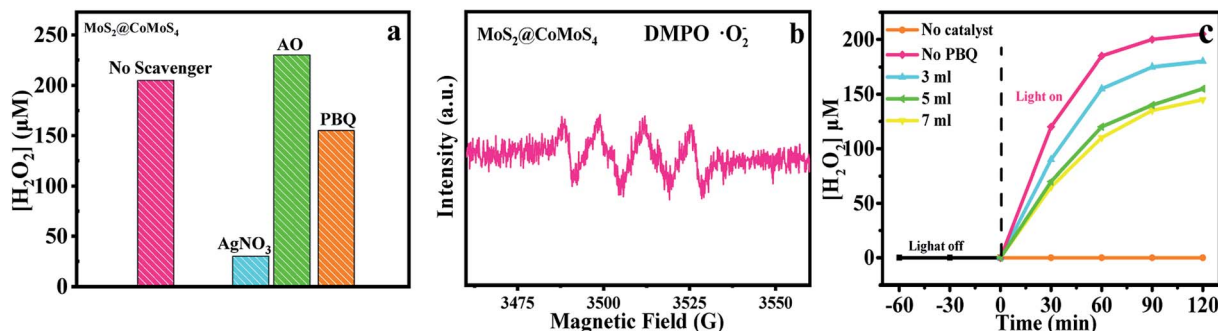


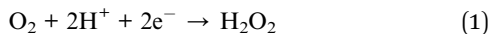
Fig. 8 (a) Free radical trapping experiments producing H_2O_2 ; (b) the DMPO spin-trapping ESR technique was used to measure the $\cdot\text{O}_2^-$ generated during H_2O_2 production; (c) the influence of PBQ content on the production of H_2O_2 on $\text{MoS}_2@\text{CoMoS}_4$.

formation of H_2O_2 and a two-step single-electron ORR might exist in the path of H_2O_2 production ((i) $\text{e}^- + \text{O}_2 = \cdot\text{O}_2^-$, -0.33 V vs. NHE; (ii) $\cdot\text{O}_2^- + \text{e}^- + 2\text{H}^+ \rightarrow \text{H}_2\text{O}_2$, 1.44 V vs. NHE). Therefore, DMPO spin-trap ESR technology was used to further detect $\cdot\text{O}_2^-$. As shown in Fig. 8b, the characteristic peaks of DMPO- $\cdot\text{O}_2^-$ were clearly observed during H_2O_2 production employing $\text{MoS}_2@\text{CoMoS}_4$, which indicated that $\cdot\text{O}_2^-$ was a probable intermediate during the H_2O_2 generation process. The ESR results strongly implied the existence of the two-step single-electron ORR using an $\cdot\text{O}_2^-$ radical as an intermediate.

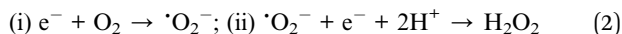
The yields of H_2O_2 with different amounts of *p*-benzoquinone (PBQ, 1 mM) were also investigated in Fig. 8c. When the content of PBQ gradually increased, the yield of H_2O_2 gradually decreased, and when the content of PBQ continued to increase to 7 mL, the amount of H_2O_2 was almost unchanged, indicating that $\cdot\text{O}_2^-$ would affect the production of H_2O_2 within a certain small range, but it could not completely suppress the production of H_2O_2 . Therefore, it was speculated that there might also exist a one-step two-electron ORR during the production of H_2O_2 ($\text{O}_2 + 2\text{H}^+ + 2\text{e}^- \rightarrow \text{H}_2\text{O}_2$, 0.68 V vs. NHE).

Based on the above test results, the two-electron one-step oxygen reduction route might dominate the entire H_2O_2 production process, but the sequential one-electron two-step oxygen reduction route may also exist. Therefore, it could be clearly proved that the *in situ* H_2O_2 generation pathway was the dominant two-electron one-step oxygen reduction route with the assistance of a sequential one-electron two-step oxygen reduction route. Therefore, the H_2O_2 production reaction in this PEC process could be described as follows:

2e^- one-step ORR



1e^- two-step ORR



Enhanced PEC performance of 2D/3D $\text{MoS}_2@\text{CoMoS}_4$ was likely to be attributable to the unique structural features reducing the charge transfer path length, the higher specific surface area of $\text{MoS}_2@\text{CoMoS}_4$ providing an increased number of PEC active sites and the optimal loading of MoS_2 restraining the recombination of e^-/h^+ pairs.

It can be seen from Fig. 7a that the amount of H_2O_2 produced gradually increased with time, and the formation rate gradually slowed down and the yield of H_2O_2 tended to stabilize, suggesting that PEC H_2O_2 production was hindered at high concentrations of H_2O_2 . This phenomenon might be caused by the *in situ* decomposition behavior of H_2O_2 . Usually, H_2O_2 can be decomposed in two ways ((i) $\text{H}_2\text{O}_2 + \text{H}^+ + \text{e}^- \rightarrow \text{H}_2\text{O} + \text{OH}^*$, $\text{H}_2\text{O}_2 + 2\text{H}^+ + 2\text{e}^- \rightarrow 2\text{H}_2\text{O}$; (ii) $\text{H}_2\text{O}_2 + \text{h}^+ \rightarrow \text{H}^+ + \text{HO}_2^*$, $\text{H}_2\text{O}_2 + 2\text{h}^+ \rightarrow 2\text{H}^+ + \text{O}_2$), where H^+/e^- is the main cause of H_2O_2 decomposition at lower pH and light-induced h^+ is the main cause of H_2O_2 decomposition at higher concentration.^{16,20,51-53}

In Fig. 7c, when the pH was further decreased to 2, the H_2O_2 decreased relatively in content, suggesting that a lower pH induced the gradual oxidation of the produced H_2O_2 into H_2O due to excess protons ($\text{H}_2\text{O}_2 + 2\text{H}^+ + 2\text{e}^- \rightarrow 2\text{H}_2\text{O}$). The above phenomena showed that although increasing the protonic acid concentration in the solution would increase the content of H_2O_2 formation, it would also greatly aggravate the *in situ* decomposition behavior of H_2O_2 , resulting in a decrease in the content of H_2O_2 . In order to further understand the *in situ* decomposition behavior of H_2O_2 , H_2O_2 (2 mM) decomposition tests were performed with all the catalysts under light illumination. As shown in Fig. 9a, there were 17%, 13% and 10% H_2O_2 decomposition over $\text{MoS}_2@\text{CoMoS}_4$, CoMoS_4 and MoS_2 after 120 min of illumination, but the decomposition of H_2O_2 was only 2% without a catalyst. The kinetic behaviors of H_2O_2 formation and decomposition could be evaluated by fitting the data of Fig. 7a and 9a. The formation and decomposition of H_2O_2 could be well fitted with the pseudo-zero-order and first-order kinetic models (Fig. 9b and c). The values of production rate (K_f) and decomposition rate (K_d) were obtained, and comparison results were shown in Fig. 9d. The K_f value was greatly improved after 2D MoS_2 coupling with 3D CoMoS_4 , and 2D/3D $\text{MoS}_2@\text{CoMoS}_4$ exhibited the largest K_f and a relatively lower K_d , leading to the highest conversion efficiency of H_2O_2 , while MoS_2 and CoMoS_4 presented lower K_f and relatively larger K_d , causing the worst yield of H_2O_2 . The results indicated that the increased specific surface area of CoMoS_4 due to the merging of 2D MoS_2 could enhance H_2O_2 production and stabilize the formed H_2O_2 under light irradiation.

As a dangerous chemical, *p*-nitrophenol (*p*-NP) is highly toxic and carcinogenic, and can cause irreversible harm to the

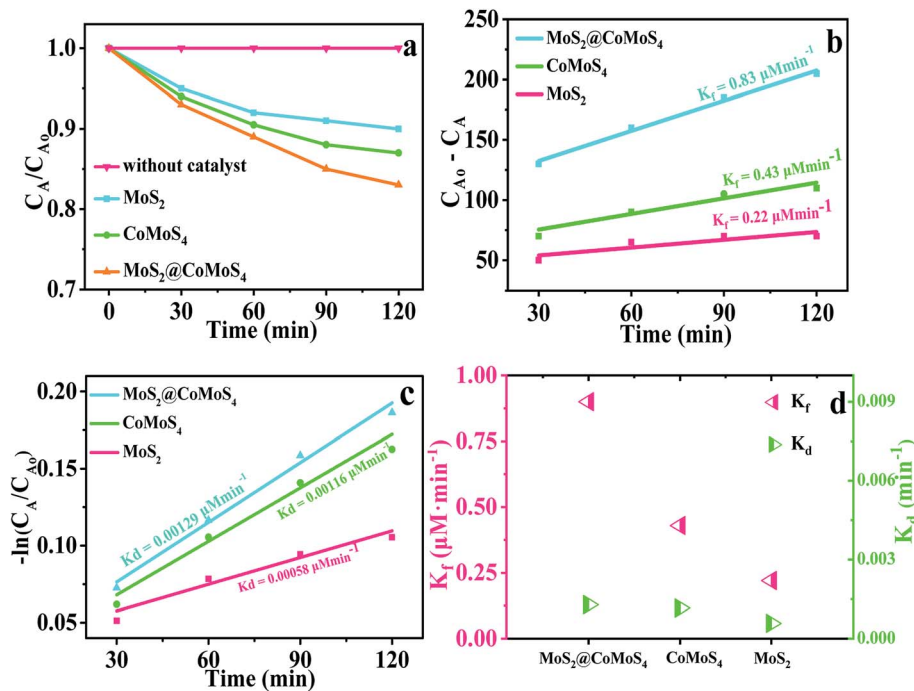


Fig. 9 The PEC decomposition of H_2O_2 (2 mM) (a); The kinetic curves of PEC H_2O_2 formation (b) and decomposition (c); formation rate constants (K_f) and decomposition rate constants (K_d) for H_2O_2 (d).

environment and human health. Therefore, the PEC conversion of toxic *p*-NP into value-added commodity chemical *p*-AP has become a top priority. *p*-AP as an organic intermediate can be widely used in the production of various medicines, dyes, antioxidants and oil additives. Therefore, reducing *p*-NP to *p*-AP is very valuable for environmental protection and industrial production. The transformation of toxic organic pollutants to low-cost and green synthetic regimes is socioeconomically important, underpinning the sustainable energy and environmental future that deserves the increasing attention of scientific communities.

The PEC reduction performances of the prepared 2D/3D $\text{MoS}_2@/\text{CoMoS}_4$ as a photocathode was also investigated by reducing *p*-NP to *p*-AP under irradiation for 180 min. It could be observed from Fig. 10a that the UV absorption spectrum peak of *p*-NP (~ 318 nm) gradually decreased with a prolongation of the

irradiation time. Clearly, compared to pure MoS_2 and CoMoS_4 , the $\text{MoS}_2@/\text{CoMoS}_4$ hybrid showed the highest PEC performance (pH = 3) (Fig. 10b). The reduction efficiency for *p*-NP was 92% after 180 min on the 2D/3D $\text{MoS}_2@/\text{CoMoS}_4$ photoelectrode. Moreover, the reduction reaction kinetic data over $\text{MoS}_2@/\text{CoMoS}_4$ composites in Fig. 10c were consistent with pseudo-first-order kinetics based on the Langmuir-Hinshelwood model, and the corresponding kinetic constant (k) was estimated to be 0.0147 min^{-1} , which was 6.13 and 3.27 times higher than for pure MoS_2 ($k = 0.0024 \text{ min}^{-1}$) and CoMoS_4 ($k = 0.0045 \text{ min}^{-1}$). The above results strongly indicated that the $\text{MoS}_2@/\text{CoMoS}_4$ thin-film electrode exhibited satisfactory PEC performance in reducing *p*-NP.

The reduction products of *p*-NP at different times were explored by HPLC analysis. The chromatographic peaks appearing at 2.98 and 1.98 min corresponded to *p*-NP and *p*-AP

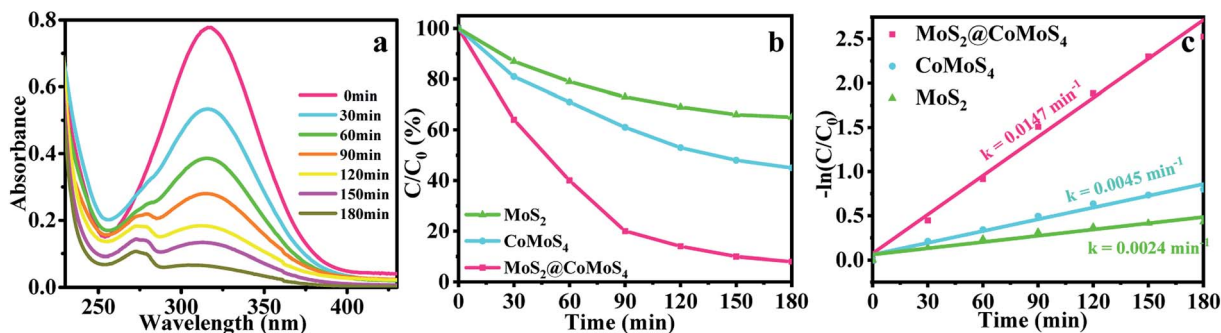


Fig. 10 (a) UV spectrum of $\text{MoS}_2@/\text{CoMoS}_4$ for *p*-NP reduction; (b) the PEC activities of as-prepared different samples and (c) the corresponding kinetic analysis.

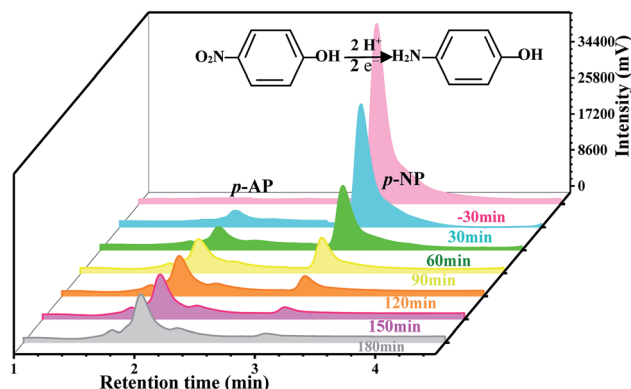


Fig. 11 Evolution of HPLC chromatograms during reduction of *p*-NP to *p*-AP with MoS₂@CoMoS₄.

standards (Fig. S4[†]). As shown in Fig. 11, the chromatographic peak appearing at 2.98 min gradually decreased as the irradiation time increased, indicating that *p*-NP was rapidly reduced. Simultaneously, a new chromatographic peak appeared at 1.98 min and gradually increased along with the increase in irradiation time, indicating that the *p*-AP yield was gradually increased. The above experimental results showed that *p*-NP was successfully converted into *p*-AP in the presence of MoS₂@CoMoS₄ under visible light irradiation. In addition, the resolution (*R*) of *p*-AP and *p*-NP was 3.93, indicating that the two compounds could be separated under the same HPLC conditions to quantify the content of the product. According to the

external standard method, the yield of *p*-AP was calculated to be about 83%. The deduced equation of the chemical reaction process has been inserted in Fig. 11.

3.3 PEC activity towards LOM degradation using an MoS₂@CoMoS₄ photoanode

The PEC degradation performance of as-obtained 2D/3D MoS₂@CoMoS₄ as a photoanode was evaluated by LOM degradation under visible light illumination for 180 min. The corresponding UV characteristic peaks of LOM were located at 280 nm and 327 nm, and the peak intensities decreased gradually with prolonged irradiation time (Fig. 12a). It could be seen that the MoS₂@CoMoS₄ composite exhibited an improved PEC activity compared to pure MoS₂ and CoMoS₄, and the percentage of LOM degradation over MoS₂@CoMoS₄ was found to be 79% (Fig. 12b) within 180 min of irradiation. Meanwhile, the oxidation reaction kinetic data over MoS₂@CoMoS₄ composites in Fig. 12c were consistent with pseudo-first-order kinetics based on the Langmuir–Hinshelwood model, and the corresponding kinetic constant (*k*) was estimated to be 0.00863 min⁻¹, which was about 1.87 and 3.17 times higher than those of pure CoMoS₄ (0.00461 min⁻¹) and MoS₂ (0.00272 min⁻¹). In addition, the degradation products of LOM after 180 min of reaction were also detected by ion chromatography. As shown in Fig. 12d, with the increase in visible light irradiation time, two new ion peaks appeared at 7.1 min and 10.4 min, which were found to be NO₃⁻ and SO₄²⁻, respectively.

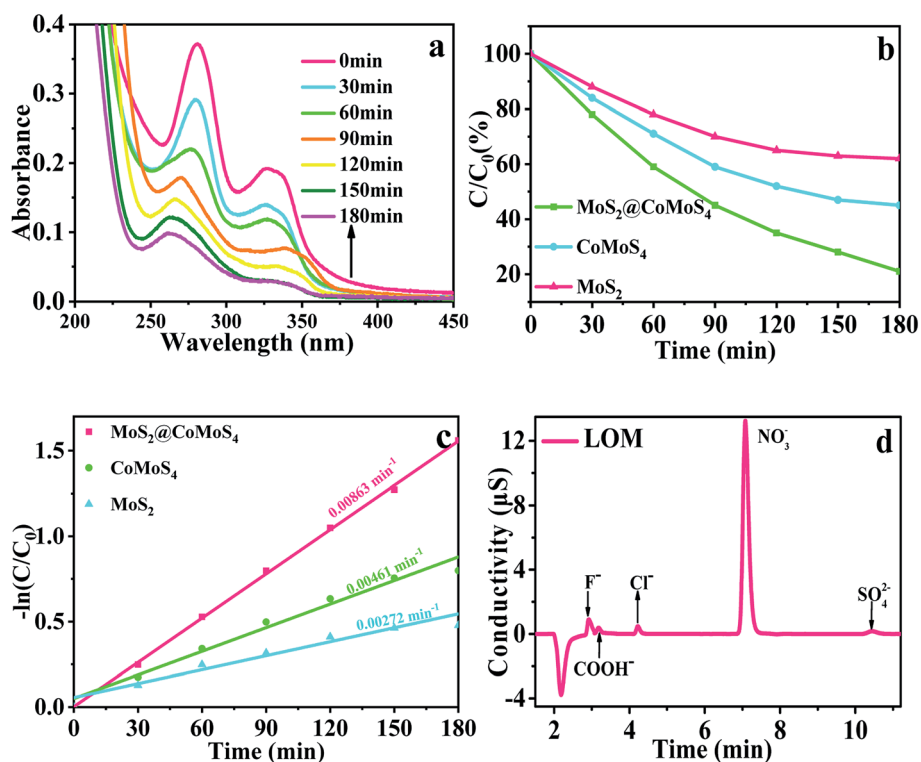


Fig. 12 (a) UV-vis spectrum of MoS₂@CoMoS₄ for LOM degradation (pH = 10); (b) The PEC activity of as-prepared different samples and (c) the corresponding kinetic analysis; (d) ion chromatogram of the LOM solution during degradation for 180 min.

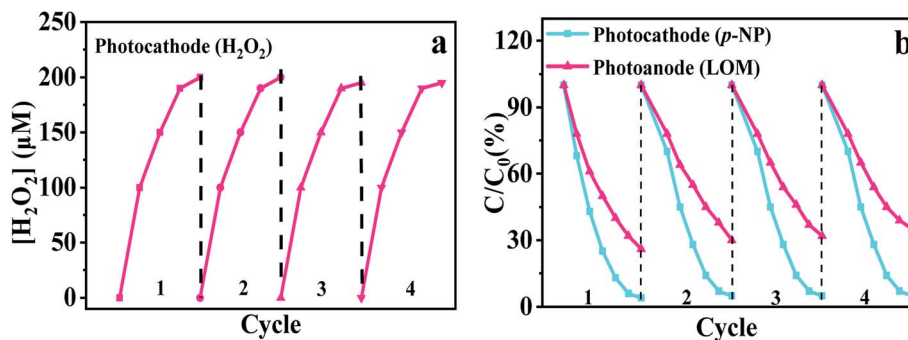


Fig. 13 Cycling runs over MoS₂@CoMoS₄ for (a) H₂O₂/(b) *p*-AP production and LOM degradation.

These results suggested that the LOM molecules were gradually converted to CO₂, H₂O and some harmless ions.

3.4 Stability

To research the stability of MoS₂@CoMoS₄ for photoelectron-driven H₂O₂/*p*-AP production and LOM degradation, recycling tests were carried out. First, the photoelectrode was washed and dried, and subsequently reused in a new system for monitoring H₂O₂/*p*-AP generation and LOM degradation under the same conditions. Fig. 13 shows that MoS₂@CoMoS₄ had excellent stability after four cycles. All of these results indicated that the PEC activity of CoMoS₄ had been further improved after forming a Z-scheme 2D/3D MoS₂@CoMoS₄ hybrid.

3.5 PEC mechanism

Based on the band gap values in Fig. 5c, MoS₂ and CoMoS₄ could be activated under visible light to generate e⁻ and h⁺ simultaneously. Generally, if the heterojunction formed between CoMoS₄ and MoS₂ was type-II, the photo-generated e⁻ on the E_{CB} of MoS₂ would be transferred to the E_{CB} of CoMoS₄ and the photo-generated h⁺ on the E_{VB} of CoMoS₄ would be transferred to the E_{VB} of MoS₂. In this way, the e⁻ accumulated on the E_{CB} of CoMoS₄ could not reduce O₂ to [•]O₂⁻, owing to the E(O₂ → [•]O₂⁻) (-0.33 eV vs. NHE) being more negative than the E_{CB} of CoMoS₄ (-0.19 eV vs. NHE), which was inconsistent with trapping experiments (Fig. 14). As shown in Fig. 14, [•]O₂⁻ was

found to be the active species in the process of H₂O₂ production and LOM degradation. Based on the above analyses, a Z-scheme PEC mechanism was proposed (Scheme 2), which is consistent with the principle of interfacial band bending.⁵⁴ In the tight solid-solid contact heterojunction interface between MoS₂ and CoMoS₄, the E_{CB} of CoMoS₄ is very close to the E_{VB} of MoS₂, providing a shorter electron transfer path, and the photo-generated e⁻ at the E_{CB} of CoMoS₄ could quickly migrate to the E_{VB} of MoS₂ and immediately combine with the h⁺ there. Thereby, the longevity of the remaining e⁻ (E_{CB,MoS₂/h⁺ (E_{VB,CoMoS₄) pairs was greatly prolonged, giving the heterojunction excellent oxidation and reduction activity. When MoS₂@CoMoS₄ was applied as a photocathode, the H₂O₂ was produced in two ways, one was by combining O₂ with 2e⁻ to directly synthesize H₂O₂, and the other one was first combining 1e⁻ to produce [•]O₂⁻ medium, and then indirectly generating H₂O₂. At the same time, the photoexcited e⁻ left at the E_{CB} of MoS₂ could also be acquired by *p*-NP to form *p*-AP, while the photogenerated h⁺ in the E_{VB} of CoMoS₄ would be neutralized by the electrons from the carbon cloth electrode, and then the charge carriers would be effectively separated for the further enhancement of PEC efficiency of H₂O₂/*p*-AP production. In contrast, when MoS₂@CoMoS₄ was used as photoanode, the e⁻ accumulated on the E_{CB} of MoS₂ would combine with O₂ to form [•]O₂⁻ for LOM degradation. Simultaneously, the photogenerated h⁺ were left on the E_{VB} of CoMoS₄ to enhance the PEC degradation efficiency of LOM (Scheme 2). Based on the analysis of the above results, the possible reaction equations could be proposed as follow:}}

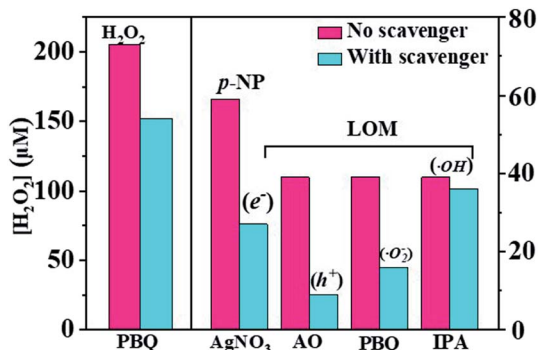
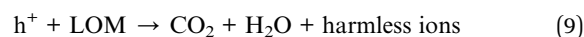
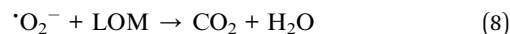
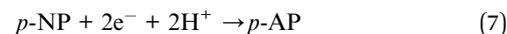
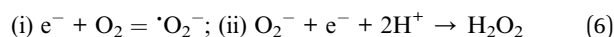
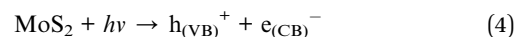
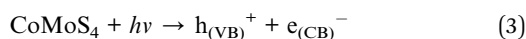
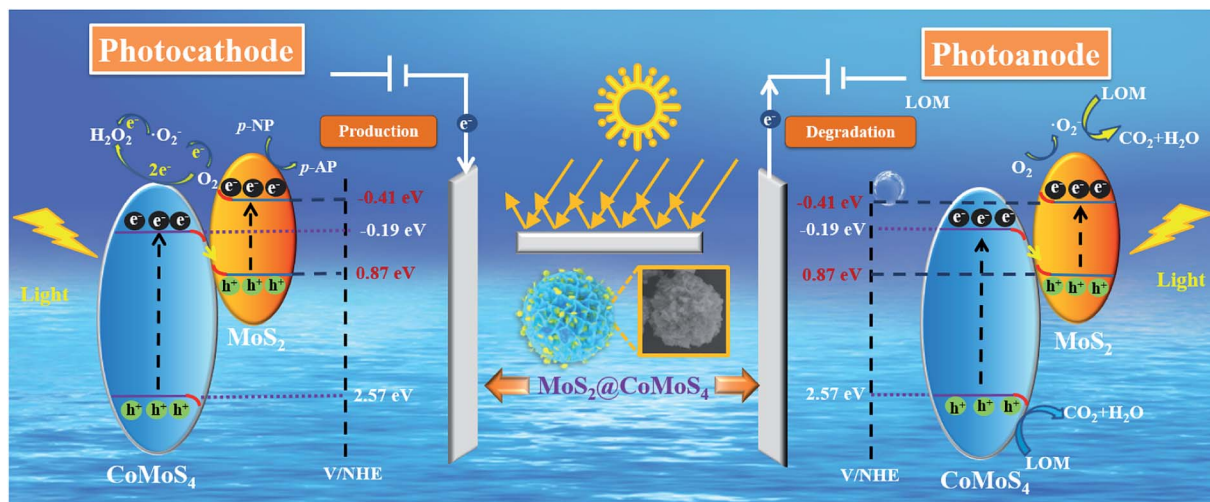


Fig. 14 The effects of various scavengers on the production of H₂O₂, reduction of *p*-NP and degradation of LOM over MoS₂@CoMoS₄.





Scheme 2 Possible PEC mechanism path.

4. Conclusions

Z-scheme 2D/3D MoS₂@CoMoS₄ flower-shaped catalyzers were fabricated *via* a hydrothermal process merging 2D MoS₂ nano-sheets into the nano-leaves of 3D CoMoS₄ micro-flowers. The construction of a rationally designed photocathode was beneficial for promoting the selective reduction of O₂ and *p*-NP to H₂O₂ and *p*-AP, respectively. With MoS₂@CoMoS₄, this supplied an economic, efficient and green route for the photoelectric-driven high-value-added product of H₂O₂ (about 205 μM H₂O₂ was produced under irradiation for 120 min)/*p*-AP (the corresponding yield of *p*-AP was about 83% under irradiation for 180 min) by using 5.0 mg of catalyst without any co-catalyst. Moreover, rapid PEC degradation towards LOM (79%) was also achieved when MoS₂@CoMoS₄ acted as a photoanode. This work could provide new insights into the rational design of a PEC system with efficient H₂O₂/*p*-AP production and capacity to degrade contaminants.

Conflicts of interest

There are no conflicts to declare.

Acknowledgements

This project was supported by the National Natural Science Foundation of China (NSFC 51672116 and 52072164), and Liao Ning Revitalization Talents Program (No. XLYC1902066). The authors also thank their colleagues and other students who participated in this study.

References

- 1 H. B. Gray, *Nature Chem.*, 2009, **1**, 7.
- 2 D. Kim, K. K. Sakimoto, D. Hong and P. Yang, *Angew. Chem. Int. Ed.*, 2015, **54**, 3259–3266.

- 3 Y. Shiraishi, S. Kanazawa, Y. Sugano, D. Tsukamoto, H. Sakamoto, S. Ichikawa and T. Hirai, *ACS Catal.*, 2014, **4**, 774–780.
- 4 Y. Fu, C.-L. Dong, W. Zhou, Y.-R. Lu, Y.-C. Huang, Y. Liu, P. Guo, L. Zhao, W.-C. Chou and S. Shen, *Appl. Catal., B*, 2020, **260**, 118206.
- 5 J. Wang, C. Xue, W. Yao, J. Liu, X. Gao, R. Zong, Z. Yang, W. Jin and D. Tao, *Appl. Catal., B*, 2019, **250**, 369–381.
- 6 I. Yamanaka and T. Murayama, *Angew. Chem. Int. Ed.*, 2008, **47**, 1900–1902.
- 7 Y. Jiang, P. Ni, C. Chen, Y. Lu, P. Yang, B. Kong, A. Fisher and X. Wang, *Adv. Energy Mater.*, 2018, **8**, 1801909.
- 8 X. Shi, S. Siahrostami, G. L. Li, Y. Zhang, P. Chakthranont, F. Studt, T. F. Jaramillo, X. Zheng and J. K. Nørskov, *Nat. Commun.*, 2017, **8**, 701.
- 9 A. Verdaguier-Casadevall, D. Deiana, M. Karamad, S. Siahrostami, P. Malacrida, T. W. Hansen, J. Rossmeisl, I. Chorkendorff and I. E. Stephens, *Nano Lett.*, 2014, **14**, 1603–1608.
- 10 S. Siahrostami, A. Verdaguier-Casadevall, M. Karamad, D. Deiana, P. Malacrida, B. Wickman, M. Escudero-Escribano, E. A. Paoli, R. Frydendal, T. W. Hansen, I. Chorkendorff, I. E. Stephens and J. Rossmeisl, *Nat. Mater.*, 2013, **12**, 1137–1143.
- 11 J. S. Jirkovsky, I. Panas, E. Ahlberg, M. Halasa, S. Romani and D. J. Schiffrin, *J. Am. Chem. Soc.*, 2011, **133**, 19432–19441.
- 12 C. H. Choi, M. Kim, H. C. Kwon, S. J. Cho, S. Yun, H. T. Kim, K. J. Mayrhofer, H. Kim and M. Choi, *Nat. Commun.*, 2016, **7**, 10922.
- 13 R. Shen, W. Chen, Q. Peng, S. Lu, L. Zheng, X. Cao, Y. Wang, W. Zhu, J. Zhang, Z. Zhuang, C. Chen, D. Wang and Y. Li, *Chem*, 2019, **5**, 2099–2110.
- 14 Z. Lu, G. Chen, S. Siahrostami, Z. Chen, K. Liu, J. Xie, L. Liao, T. Wu, D. Lin, Y. Liu, T. F. Jaramillo, J. K. Nørskov and Y. Cui, *Nat. Catal.*, 2018, **1**, 156–162.
- 15 P. Y. Kuang, Y. Z. Su, K. Xiao, Z. Q. Liu, N. Li, H. J. Wang and J. Zhang, *ACS Appl. Mater. Interfaces*, 2015, **7**, 16387–16394.

- 16 L. Zhou, J. Feng, B. Qiu, Y. Zhou, J. Lei, M. Xing, L. Wang, Y. Zhou, Y. Liu and J. Zhang, *Appl. Catal., B*, 2020, **267**, 118396–118404.
- 17 Y. Kofuji, S. Ohkita, Y. Shiraishi, H. Sakamoto, S. Ichikawa, S. Tanaka and T. Hirai, *ACS Sustainable Chem. Eng.*, 2017, **5**, 6478–6485.
- 18 Y. Kofuji, S. Ohkita, Y. Shiraishi, H. Sakamoto, S. Tanaka, S. Ichikawa and T. Hirai, *ACS Catal.*, 2016, **6**, 7021–7029.
- 19 Y. Yang, Z. Zeng, G. Zeng, D. Huang, R. Xiao, C. Zhang, C. Zhou, W. Xiong, W. Wang, M. Cheng, W. Xue, H. Guo, X. Tang and D. He, *Appl. Catal., B*, 2019, **258**, 117956–117966.
- 20 Y. Kofuji, Y. Isobe, Y. Shiraishi, H. Sakamoto, S. Tanaka, S. Ichikawa and T. Hirai, *J. Am. Chem. Soc.*, 2016, **138**, 10019–10025.
- 21 S. Li, G. Dong, R. Hailili, L. Yang, Y. Li, F. Wang, Y. Zeng and C. Wang, *Appl. Catal., B*, 2016, **190**, 26–35.
- 22 H. Kim, S. Gim, T. H. Jeon, H. Kim and W. Choi, *ACS Appl. Mater. Interfaces*, 2017, **9**, 40360–40368.
- 23 E. V. Kondratenko, G. Mul, J. Baltrusaitis, G. O. Larrazábal and J. Pérez-Ramírez, *Energy Environ. Sci.*, 2013, **6**, 3112–3135.
- 24 B. Klahr, S. Gimenez, F. Fabregat-Santiago, J. Bisquert and T. W. Hamann, *J. Am. Chem. Soc.*, 2012, **134**, 16693–16700.
- 25 Y.-J. Yuan, Z. Li, S. Wu, D. Chen, L.-X. Yang, D. Cao, W.-G. Tu, Z.-T. Yu and Z.-G. Zou, *Chem. Eng. J.*, 2018, **350**, 335–343.
- 26 J. Liang, Y. Jiao, M. Jaroniec and S. Z. Qiao, *Angew. Chem. Int. Ed.*, 2012, **51**, 11496–11500.
- 27 L. Zheng, H. Su, J. Zhang, L. S. Walekar, H. V. Molamahmood, B. Zhou, M. Long and Y. H. Hu, *Appl. Catal., B*, 2018, **239**, 475–484.
- 28 K.-H. Cho and Y.-M. Sung, *Nano Energy*, 2017, **36**, 176–185.
- 29 Q. A. Drmoseh, A. Hezam, A. H. Y. Hendi, M. Qamar, Z. H. Yamani and K. Byrappa, *Appl. Surf. Sci.*, 2020, **499**, 143938.
- 30 G. Yang, D. Chen, H. Ding, J. Feng, J. Z. Zhang, Y. Zhu, S. Hamid and D. W. Bahnemann, *Appl. Catal., B*, 2017, **219**, 611–618.
- 31 J. Staszak-Jirkovskiy, C. D. Malliakas, P. P. Lopes, N. Danilovic, S. S. Kota, K. C. Chang, B. Genorio, D. Strmcnik, V. R. Stamenkovic, M. G. Kanatzidis and N. M. Markovic, *Nat. Mater.*, 2016, **15**, 197–203.
- 32 Y. Sun, C. Wang, T. Ding, J. Zuo and Q. Yang, *Nanoscale*, 2016, **8**, 18887–18892.
- 33 L. Yang, Y. Hu and L. Zhang, *Chem. Eng. J.*, 2019, **378**, 122092.
- 34 L. Zhang, Y. Hu and J. Zheng, *J. Mater. Chem. A*, 2017, **5**, 18664–18673.
- 35 L. Jing, Y. Xu, S. Huang, M. Xie, M. He, H. Xu, H. Li and Q. Zhang, *Appl. Catal., B*, 2016, **199**, 11–22.
- 36 X. Yang, F. Qian, G. Zou, M. Li, J. Lu, Y. Li and M. Bao, *Appl. Catal., B*, 2016, **193**, 22–35.
- 37 M. Wei, C. Wang, Y. Yao, S. Yu, W.-H. Liao, J. Ren, R. Sun and C.-P. Wong, *Chem. Eng. J.*, 2019, **355**, 891–900.
- 38 S. Wang, D. Zhang, B. Li, C. Zhang, Z. Du, H. Yin, X. Bi and S. Yang, *Adv. Energy Mater.*, 2018, **8**, 1801345.
- 39 X. Xu, Y. Song, R. Xue, J. Zhou, J. Gao and F. Xing, *Chem. Eng. J.*, 2016, **301**, 266–275.
- 40 X. Y. Yu, Y. Feng, Y. Jeon, B. Guan, X. W. Lou and U. Paik, *Adv. Mater.*, 2016, **28**, 9006–9011.
- 41 Y. R. Liu, X. Shang, W. K. Gao, B. Dong, X. Li, X. H. Li, J. C. Zhao, Y. M. Chai, Y. Q. Liu and C. G. Liu, *J. Mater. Chem. A*, 2017, **5**, 2885–2896.
- 42 J. Zheng and L. Zhang, *Appl. Catal., B*, 2018, **231**, 34–42.
- 43 X. Dai, K. Du, Z. Li, M. Liu, Y. Ma, H. Sun, X. Zhang and Y. Yang, *ACS Appl. Mater. Interfaces*, 2015, **7**, 27242–27253.
- 44 Y.-R. Liu, X. Shang, W.-K. Gao, B. Dong, J.-Q. Chi, X. Li, K.-L. Yan, Y.-M. Chai, Y.-Q. Liu and C.-G. Liu, *Appl. Surf. Sci.*, 2017, **412**, 138–145.
- 45 Q. Li, X.-Q. Qiao, Y. Jia, D. Hou and D.-S. Li, *ACS Appl. Nano Mater.*, 2019, **3**, 68–76.
- 46 J. Luo, G. Dong, Y. Zhu, Z. Yang and C. Wang, *Appl. Catal., B*, 2017, **214**, 46–56.
- 47 Q. Li, X.-Q. Qiao, Y. Jia, D. Hou and D.-S. Li, *Appl. Surf. Sci.*, 2019, **498**, 143863.
- 48 S. Hua, D. Qu, L. An, W. Jiang, Y. Wen, X. Wang and Z. Sun, *Appl. Catal., B*, 2019, **240**, 253–261.
- 49 W. Shi, F. Guo, H. Wang, M. Han, H. Li, S. Yuan, H. Huang, Y. Liu and Z. Kang, *Appl. Catal., B*, 2017, **219**, 36–44.
- 50 W. Zou, Y. Shao, Y. Pu, Y. Luo, J. Sun, K. Ma, C. Tang, F. Gao and L. Dong, *Appl. Catal., B*, 2017, **218**, 51–59.
- 51 X. Wang, Z. Han, L. Yu, C. Liu, Y. Liu and G. Wu, *ACS Sustainable Chem. Eng.*, 2018, **6**, 14542–14553.
- 52 S. Thakur, T. Kshetri, N. H. Kim and J. H. Lee, *J. Catal.*, 2017, **345**, 78–86.
- 53 Y. Shiraishi, S. Kanazawa, Y. Kofuji, H. Sakamoto, S. Ichikawa, S. Tanaka and T. Hirai, *Angew. Chem. Int. Ed.*, 2014, **53**, 13454–13459.
- 54 Z.-F. Huang, J. Song, X. Wang, L. Pan, K. Li, X. Zhang, L. Wang and J.-J. Zou, *Nano Energy*, 2017, **40**, 308–316.